1 FRONT MATTER

2

3 **Title**

4 Cells recognize osmotic stress through liquid-liquid phase separation lubricated with
5 poly(ADP-ribose)

6

7 **Authors**

8 Kengo Watanabe[1,*], Kazuhiro Morishita[1], Xiangyu Zhou[1], Shigeru Shiizaki[1], Yasuo
9 Uchiyama[2], Masato Koike[3], Isao Naguro[1], Hidenori Ichijo[1,*].

10

11 **Affiliations**

12 [1]Laboratory of Cell Signaling, Graduate School of Pharmaceutical Sciences, The
13 University of Tokyo, Tokyo 113-0033, Japan.
14 [2]Department of Cellular and Molecular Neuropathology, Juntendo University Graduate
15 School of Medicine, Tokyo 113-8421, Japan.
16 [3]Department of Cell Biology and Neuroscience, Juntendo University Graduate School of
17 Medicine, Tokyo 113-8421, Japan.
18 *Correspondence to: kwatanabe@mol.f.u-tokyo.ac.jp (K.W.), ichijo@mol.f.u-tokyo.ac.jp
19 (H.I.)

20

21 **Abstract**

22 Cells are under threat of osmotic perturbation; and cell volume maintenance is critical in
23 cerebral edema, inflammation and aging, in which prominent changes in intracellular or
24 extracellular osmolality emerge. After osmotic stress-enforced cell swelling or shrinkage,
25 the cells regulate intracellular osmolality to recover their volume. However, the
26 mechanisms recognizing osmotic stress remain obscured. We previously clarified that
27 apoptosis signal-regulating kinase 3 (ASK3) bidirectionally responds to osmotic stress
28 and regulates cell volume recovery. Here, we report that macromolecular crowding
29 induces liquid-demixing condensates of ASK3 under hyperosmotic stress, which
30 transduce osmosensing signal into ASK3 inactivation. A genome-wide small interfering
31 RNA (siRNA) screen identified an ASK3 inactivation regulator, nicotinamide
32 phosphoribosyltransferase (NAMPT), related to poly(ADP-ribose) signaling.
33 Furthermore, we clarify that poly(ADP-ribose) keeps ASK3 condensates in the liquid
34 phase and enables ASK3 to become inactivated under hyperosmotic stress. Our findings
35 demonstrate that cells rationally incorporate physicochemical phase separation into their
36 osmosensing systems.

37

38

39 **MAIN TEXT**

40

41 **Introduction**

42 When a difference between intracellular and extracellular osmolality develops, cells
43 inevitably become swollen or shrunken following osmotically driven water flow. The
44 abnormal cellular osmoregulation leads to deteriorated pathophysiological conditions
45 observed in cerebral edema, inflammation, cataracts and aging (*1–7*). Basically,
46 homeostasis in cell volume is vital for cellular activities and cells have a defense system
47 against the disastrous osmotic stress; cells immediately excrete or intake ions and small
48 organic solutes after hypoosmotic or hyperosmotic stresses, respectively, and recover
49 their volume within minutes to hours by controlling ion channels and transporters (*8–10*).
50 Many electrophysiological and pharmacological studies have contributed to the
51 accumulation of knowledge about the effector molecules in cell volume regulation. In
52 contrast, the mechanisms sensing osmotic stress to induce cell volume recovery remain
53 unclear, especially in mammalian cells. Similar to the osmosensors proposed in bacteria,
54 yeasts and plants (*11–13*), mechanical changes in/on the cell membrane have recently
55 drawn attention in mammalian cells; for example, membrane stretching under
56 hypoosmotic stress activates mechanosensitive channels such as the transient receptor
57 potential (TRP) channel V4 (*14, 15*). This mechanism can be illustrated by an easy-to-
58 understand signaling schematic with arrows directed from the extracellular side to the
59 intracellular side. However, osmotic stress perturbs not only the cell membrane but also
60 the intracellular ion strength/concentration and macromolecular crowding (*8, 9*);
61 therefore, the existence of intracellular osmosensors may currently be underestimated.

62 We previously reported that apoptosis signal-regulating kinase 3 (ASK3; also known
63 as MAP3K15) is phosphorylated and activated under hypoosmotic stress and conversely
64 dephosphorylated and inactivated under hyperosmotic stress (*16*). Furthermore, in
65 addition to the rapid, sensitive and reversible nature, this bidirectional response of ASK3
66 orchestrates proper cell volume recovery under both hypoosmotic and hyperosmotic
67 stresses (*17*). Therefore, we conceived that the elucidation of ASK3 regulation under
68 osmotic stress would lead to the clarification of a general mammalian osmosensing
69 system. In this study, we report that ASK3 forms liquid droplets under hyperosmotic
70 stress, which is necessary for ASK3 inactivation. Moreover, by utilizing a genome-wide
71 small interfering RNA (siRNA) screen, we reveal that poly(ADP-ribose) (PAR)
72 maintains the liquidity of ASK3 droplets for ASK3 inactivation. Our findings reveal that
73 cells recognize osmotic stress by utilizing liquid-liquid phase separation (LLPS) of ASK3
74 with the support of PAR.

75

76 **Results**

77 **Hyperosmotic stress induces ASK3 condensation through liquid-liquid phase**
78 **separation**

79 Through analyses of ASK3, we found that the subcellular localization of ASK3
80 drastically changes under hyperosmotic stress: a part of ASK3 diffuses throughout the
81 cytosol, while the other forms granule-like structures, ASK3 condensates (Fig. 1A). The
82 number of ASK3 condensates increased in a hyperosmolality strength-dependent manner

83   (Fig. 1B) and gradually diminished several dozen minutes after hyperosmotic stress (Fig.
84   S1A and B), which corresponds to the time range of cell volume recovery (*10*, *17*). In
85   addition to mannitol-supplemented medium, sodium chloride-supplemented medium
86   induced a similar pattern of ASK3 localization (Fig. S1C and D), suggesting that
87   hyperosmolality causes ASK3 condensates. Counterintuitively, the size of condensates
88   was inversely correlated with hyperosmolality (Fig. 1B). In fact, a simple computational
89   model (*18*) predicted that the size of ASK3 clusters would increase as the grid space is
90   reduced, mimicking cell shrinkage under hyperosmotic stress (Fig. S1E and F, see also
91   Supplementary Text). However, there are abundant macromolecules in cells (*19*); and we
92   modified the model by adding obstacles (Fig. S1G). Our simulation results demonstrated
93   that decreasing the grid space progressively increases both the number and size of ASK3
94   clusters, while further decreasing the grid space eventually reduces the size of clusters
95   after the maximum has been reached (Fig. 1C, D and Movie S1), implying that the
96   macromolecular crowding is critical for ASK3 condensates under hyperosmotic stress in
97   cells.
98   Further characterization revealed that ASK3 condensates are colocalized with a
99   marker of neither early endosomes nor lysosomes (Fig. S1H and I). Transmission
100   electron microscopy (TEM) analysis with the immunogold-labelling technique revealed
101   that ASK3 condensates are membrane-less structures (Fig. 1E). Although stress granules
102   and P-bodies are known membrane-less structures under extreme hyperosmotic
103   conditions (*20*, *21*), markers of neither structure were found to be colocalized with ASK3
104   condensates (Fig. S1J). Upon observing in 1-second intervals, we found that ASK3
105   condensates appear just seconds after hyperosmotic stress, which is much faster than in
106   the case of stress granules, and that ASK3 condensates dynamically move around and
107   fuse with each other (Fig. 1F and Movie S2). Furthermore, our computational model
108   predicted that the shrinkage-induced clusters gradually disappear when the grid space is
109   reverted back to the initial state (Fig. 1G, H and Movie S3, and Supplementary Text), and
110   we observed similar kinetics of reversibility in cells (Fig. 1I and J). Interestingly, our
111   model also predicted a transient increase in the size of clusters just after restoration to the
112   initial space, which was in good agreement with the cell-based experiments. To further
113   address the dynamics of ASK3 condensates, we established a fluorescence recovery after
114   photobleaching (FRAP) assay for the rapidly moving condensates and found that ASK3
115   condensates display not complete but significant FRAP (Fig. 1K and L), indicating that
116   ASK3 molecules in the condensates are interchanged with those in the cytosol.
117   Given these characteristics, we concluded that ASK3 condensates are liquid-demixing
118   droplets induced by LLPS (*22–24*). Indeed, according to soft matter physics, there are
119   two modes of LLPS, "nucleation and growth" and "spinodal decomposition", and we
120   observed the spinodal decomposition-like pattern of ASK3 as a rare case (Fig. S1K).
121   Additionally, crowding reagents, such as Ficoll and polyethylene glycol (PEG), induced
122   ASK3 condensates in vitro (Fig. 1M and N). Although the intracellular ion strength and
123   concentration are altered under hyperosmotic stress in cells, the change in sodium
124   chloride concentration did not induce ASK3 condensates in vitro, suggesting again that
125   molecular crowding but not ion strength is a critical driving force for the formation of
126   ASK3 condensates under hyperosmotic stress. Of note, the condensates produced by our
127   in vitro assays are solid-like because we could not observe their FRAP, but the results can

128 be extrapolated to the case in the liquid phase because the driving force in the formation
129 step would be common between the liquid-like and solid-like condensates (*22–24*).

C-terminus coiled-coil and low complexity region are required for ASK3
condensation followed by ASK3 inactivation under hyperosmotic stress

132 To clarify the significance of ASK3 condensation in cells, we first generated ASK3
133 mutants that are unable to condense. While ASK3 ΔN normally condensed, ASK3 ΔC
134 lost the ability to condense under hyperosmotic stress (Fig. 2A and B). Moreover, ASK3
135 CT formed condensates even under isoosmotic conditions, while ASK3 NT and KD did
136 not exhibit the ability to condense, suggesting that the C-terminus of ASK3 is necessary
137 and sufficient for ASK3 condensation. In the ASK3 C-terminus, 5 distinctive regions are
138 bioinformatically predicted (Fig. S2A): two intrinsically disordered regions (IDRs; Fig.
139 S2B), one coiled-coil domain (CC), one sterile alpha motif domain (SAM) (*25*) and one
140 low complexity region (LCR). Between ASK3 CT mutants with these deletions, CTΔCC,
141 CTΔSAM and CTΔLCR exhibited reduced condensation ability compared with the
142 original CT (Fig. S2C). Considering the location of LCR within SAM, we next deleted
143 both CC and SAM or LCR from ASK3 CT and found that CTΔCCΔSAM and
144 CTΔCCΔLCR are unable to condense even under hyperosmotic stress (Fig. S2D),
145 suggesting that both CC and LCR contribute to ASK3 condensation. In addition, we
146 confirmed that full-length ASK3 lacking the C-terminus CC (CCC) and LCR (CLCR)
147 cannot form condensates under hyperosmotic stress (Fig. 2C).
148 Previously, we elucidated that ASK3 is inactivated a few minutes after hyperosmotic
149 stress by protein phosphatase 6 (PP6) (*17*). Since ASK3 condensation occurs prior to its
150 inactivation, we evaluated the inactivation of ASK3 mutants lacking condensation ability.
151 Although exhibiting lower basal activities under isoosmotic conditions, ASK3 ΔC and
152 ΔCCCΔCLCR were not inactivated under hyperosmotic stress (Fig. 2D and S3A),
153 suggesting that ASK3 condensation is required for its inactivation. In fact, we discovered
154 the unique relationship between ASK3 condensates and one of the PP6 subunits
155 ANKRD52 (*17, 26*); ANKRD52 condensates are not completely colocalized with ASK3
156 condensates, but they move around and grow while sharing their phase boundaries (Fig.
157 2E and Movie S4).

Nicotinamide phosphoribosyltransferase regulates ASK3 inactivation via the NAD
salvage pathway

160 To reveal the details of ASK3 condensation and inactivation, we investigated the
161 candidate regulators of ASK3 inactivation identified by our genome-wide siRNA screen
162 (*17*). Among them, we focused on the highest-ranked and unexpected candidate
163 nicotinamide phosphoribosyltransferase (NAMPT), the rate-limiting enzyme in the
164 mammalian nicotinamide adenine dinucleotide (NAD) salvage pathway (*27*) (Fig. 3A and
165 B). NAMPT knockdown suppressed ASK3 inactivation under hyperosmotic stress (Fig.
166 3C and S3B). Additionally, NAMPT knockdown increased endogenous ASK3 activity
167 and inhibited downstream STE20/SPS1-related proline/alanine-rich kinase
168 (SPAK)/oxidative stress-responsive kinase 1 (OSR1) activities under hyperosmotic stress
169 (Fig. 3D and S3C), consistent with our previous finding that ASK3 suppresses

170   SPAK/OSR1 in a kinase activity-dependent manner (*16*). Overexpression of wild-type
171   (WT) NAMPT fully accelerated ASK3 inactivation under hyperosmotic stress in an
172   amount-dependent manner (compare lanes 8–10: Fig. 3E and S3D). In accordance with
173   the fact that NAMPT enzymatically functions as a homodimer (*28*), the homodimer-
174   insufficient mutant S199D could not fully promote ASK3 inactivation, and the
175   homodimer-null mutant S200D could not promote any ASK3 inactivation (*29*) (lanes 11–
176   14: Fig. 3E and S3D). Furthermore, the NAMPT enzymatic inhibitor FK866 (*30*)
177   inhibited ASK3 inactivation, which was canceled by further supplementation with the
178   NAMPT product nicotinamide mononucleotide (NMN) (Fig. 3F and S3E). Moreover,
179   pretreatment with FK866 and NMN suppressed and promoted the interaction between
180   ASK3 and PP6 under hyperosmotic stress, respectively (*17*) (Fig. 3G, 3H, S3F and S3G).
181   Hence, NAMPT ensures ASK3 inactivation by PP6 via the NAD salvage pathway.

182   **Poly(ADP-ribose) maintains the liquidity of ASK3 condensates for its inactivation**

183   NAD is not only a coenzyme in cellular redox reactions but also a substrate for enzymatic
184   consumers, including cADP-ribose synthase CD38/157, sirtuins and PAR polymerases
185   (PARPs) (*31*) (Fig. 3B). We thus examined the potential involvement of NAD-
186   consuming enzymes in ASK3 inactivation. In contrast to the overexpression of NAMPT
187   (Fig. 3E), neither CD38, SIRT2 nor PARP1 enhanced ASK3 inactivation under
188   hyperosmotic stress (Fig. S4A–C); rather, their overexpression even suppressed ASK3
189   inactivation, probably because they compete with the actual NAD-requiring regulators in
190   ASK3 inactivation with respect to NAD. In the dynamics of PARsylation, however, not
191   only PARP writers but also readers and erasers regulate PAR signaling (*32*, *33*) (Fig.
192   4A). Interestingly, NAMPT overexpression and FK866 pretreatment increased and
193   decreased PARsylated proteins, respectively (Fig. 4B and S3H). We therefore examined
194   the potential involvement of PAR signaling in ASK3 inactivation by controlling an eraser
195   PAR glycohydrolase (PARG). PARG overexpression partially suppressed ASK3
196   inactivation under hyperosmotic stress, while the glycohydrolase-inactive mutant
197   E673A/E674A (*34*) did not (Fig. 4C and S3I), suggesting that PARsylation by
198   unidentified PARP(s) or PAR per se is required for ASK3 inactivation under
199   hyperosmotic stress.
200   PAR physicochemically resembles RNA. In addition to RNA, PAR is proposed to
201   seed condensates (*35–38*). Considering that ASK3 condensation is required for its
202   inactivation (Fig. 2), we next investigated the relationship between PAR and ASK3
203   condensation. Contrary to our expectation, ASK3 condensation under hyperosmotic
204   stress was not prevented by PAR depletion with FK866 pretreatment or PARG
205   overexpression (Fig. 4D). However, FRAP of ASK3 condensates was significantly
206   inhibited by PAR depletion (Fig. 4E and F). Furthermore, PAR inhibited the formation of
207   solid-like ASK3 condensates in vitro, while NAD could not (Fig. 4G and H). These
208   results raise the possibility that PAR does not seed but rather lubricates phase-separated
209   ASK3 for ASK3 inactivation.
210   As a consensus sequence of the PAR-binding motif (PBM), $[HKR]_1-X_2-X_3-$
211   $[AIQVY]_4-[KR]_5-[KR]_6-[AILV]_7-[FILPV]_8$ is proposed (*39*). Based on the difference
212   between ASK3 WT and CT in condensation at the basal state (Fig. 2B), some kind of
213   inhibitory region is assumed to be present in the region before the C-terminus of ASK3,

214   where the central positively charged $[KR]_5$-$[KR]_6$ is found in 10 sites, named PBM1–10
215   (Fig. S5A). We thus constructed 10 PBM candidate mutants substituted K/R with A. All
216   PBM candidate mutants of ASK3 formed condensates under hyperosmotic stress (Fig.
217   S5B). Between them, the ASK3 PBM4 mutant prominently suppressed its inactivation
218   under hyperosmotic stress (Fig. S5C). Indeed, while ASK3 WT was
219   coimmunoprecipitated with PAR by pull-down of the WWE domain (*40*) (Fig. 4A), the
220   PBM4 mutant was not (Fig. S5D), suggesting that ASK3 interacts with PAR via the
221   PBM4 region. Consistent with PAR depletion (Fig. 4E), FRAP of the ASK3 PBM4
222   mutant was significantly suppressed (Fig. S5E and F). Moreover, the solid-like
223   condensates of the ASK3 PBM4 mutant in vitro were not dissolved by PAR addition
224   (Fig. S5G and H). These findings reinforce the notion that PAR keeps ASK3 condensates
225   in the liquid phase, enabling ASK3 to be inactivated under hyperosmotic stress.

226

Discussion

227
228   In general, cells face three types of perturbations after osmotic stress: changes in
229   mechanical forces in/on the phospholipid bilayer, intracellular strength/concentration of
230   ions and macromolecular crowding (*9*). It has been suggested that cells recognize
231   unsubstantial osmotic stress through these changes. Here, we demonstrated that an
232   osmoresponsive kinase quickly forms liquid-demixing condensates after hyperosmotic
233   stress, followed by the regulation of its kinase activity. Our computational model and in
234   vitro assays suggested that the change in macromolecular crowding is a driving force for
235   the condensation. Although many researchers have recently been seeking osmosensors
236   in/on the cell membrane, our findings shed light on another mechanism that cells sense
237   osmotic stress from the inside through LLPS. Our findings are reflective of a theory put
238   forth in 1987, when Zimmerman and Harrison proposed "*Changes in reaction rates due*
239   *to changes in crowding provide, in principle, a simple mechanism by which the cell could*
240   *sense changes in its own volume*" (*41*). We can advance upon and generalize their idea:
241   cells naturally recognize changes in their volume through phase separation/transition
242   triggered by changes in macromolecular crowding.
243   Recent studies on LLPS have gradually unveiled the versatile functions of
244   biomolecular condensates, including the acceleration or suppression of specific reactions,
245   the buffering effects on specific biomolecule concentrations, and even the selective filters
246   of nuclear pores (*22*, *23*, *42*). In this study, we reported the dual function of ASK3
247   condensates. One function involves the sensing machinery for osmotic stress. Stress-
248   sensing condensates were also suggested in yeast under thermal or pH stresses (*43*).
249   Interestingly, all of these stresses are bidirectionally induced by deviation from steady
250   state; thus, the role of liquid-demixing droplets would be rational in quick and reversible
251   stress recognition. The other is the dephosphorylation/inactivation of ASK3. Because the
252   dephosphorylation competes with the autophosphorylation of ASK3 at the basal level,
253   this would be interpreted as not the trigger of the reaction but the acceleration of the
254   reaction specificity. As another possibility, however, ASK3 condensates may serve as
255   multifunctional signaling hubs for the whole regulation of ASK3 activity. In fact, the
256   ASK3 mutants ΔC and ΔCCCΔCLCR, which are unable to form condensates, exhibited
257   lower kinase activity even under basal conditions (Fig. 2D). Although our confocal
258   microscopy detected few ASK3 condensates under isoosmotic conditions (Fig. 1A), our

259   computational simulation indicated that small clusters appear stochastically and
260   transiently under larger grid space (Fig. 1C and Movie S1), which may be related to a
261   report on local phase separation (*44*). To explore this possibility, further analyses, such as
262   the identification of biomolecules within the ASK3 condensates, are needed.
263   PAR consists of three components—a base (adenine), ribose and phosphate—which
264   are the same as RNA. In many biomolecular condensates, RNA promotes LLPS of RNA-
265   binding proteins (RBPs) partly because the interaction between RNA and RBPs reduces
266   the threshold for LLPS (*22–24*). Likewise, PAR has been reported to promote
267   condensation (*36–38*). In contrast, we described that PAR is not a promoter of ASK3
268   condensates but rather a lubricator. By keeping the liquidity of ASK3 condensates within
269   the "Goldilocks zone", PAR provides the opportunity for interaction between ASK3 and
270   PP6 followed by ASK3 inactivation; otherwise, ASK3 condensates undergo liquid-to-
271   solid transition (Fig. 4E and S5E), analogous to prion-like RBPs (*45*).
272

Materials and Methods

274   The key materials used in this study are summarized in Table S1.
275

Reagents

277   FK866 (Cat. #F8557) and β-nicotinamide mononucleotide (NMN; Cat. #N3501) were
278   purchased from Sigma-Aldrich and dissolved at a final concentration of 1,000x in
279   dimethyl sulfoxide (DMSO; Sigma-Aldrich, Cat. #D5879) and ultrapure water,
280   respectively. The solvents were used as each negative control.
281

Expression plasmids and siRNAs

283   Expression plasmids for this study were constructed by standard molecular biology
284   techniques, and all constructs were verified by sequencing. Human ASK3 cDNA (CDS of
285   NM_001001671.3 with c.147C>T, c.574G>A) was previously cloned and subcloned into
286   pcDNA3/GW (Invitrogen) with an N-terminal FLAG- or HA-tag (*16*) or into
287   pcDNA4/TO (Invitrogen) with an N-terminal FLAG- or EGFP-tag (*17*). Human ASK3
288   cDNA was also subcloned into pcDNA3 with a C-terminal tdTomato-tag (cDNA was
289   gifted by M. Davidson, Florida State University, via Addgene: plasmid #54653) or
290   pcDNA4/TO with an N-terminal Venus- or EGFP-FLAG-tag. EGFP-FLAG-tag was
291   constructed by connecting EGFP-tag and FLAG-tag with a Gly-Gly linker and subcloned
292   into pcDNA4/TO. ASK3 mutants ΔN (CDS of NM_001001671.3 with c.1_1,866del), ΔC
293   (CDS of NM_001001671.3 with c.147C>T, c.574G>A, c.2,734_3,939del), NT (CDS of
294   NM_001001671.3 with c.147C>T, c.574G>A, c.1,867_3,939del), KD (CDS of
295   NM_001001671.3 with c.1_1,866del, c.2,734_3,939del), CT (CDS of NM_001001671.3
296   with c.1_2,712del), ΔCCC (CDS of NM_001001671.3 with c.147C>T, c.574G>A,
297   c.3,535_3,675del), ΔCLCR (CDS of NM_001001671.3 with c.147C>T, c.574G>A,
298   c.3,838_3,879del), ΔCCCΔCLCR (CDS of NM_001001671.3 with c.147C>T,
299   c.574G>A, c.3,535_3,675del, c.3,838_3,879del), CTΔIDR1 (CDS of NM_001001671.3
300   with c.1_2,712del, c.2,788_2,898del), CTΔIDR2 (CDS of NM_001001671.3 with
301   c.1_2,712del, c.3,427_3,540del), CTΔIDRs (CDS of NM_001001671.3 with
302   c.1_2,712del, c.2,788_2,898del, c.3,427_3,540del), CTΔCC (CDS of NM_001001671.3
303   with c.1_2,712del, c.3,535_3,675del), CTΔSAM (CDS of NM_001001671.3 with
304   c.1_2,712del, c.3,718_3,909del), CTΔLCR (CDS of NM_001001671.3 with

305 c.1_2,712del, c.3,838_3,879del), CTΔCCΔSAM (CDS of NM_001001671.3 with
306 c.1_2,712del, c.3,535_3,675del, c.3,718_3,909del), CTΔCCΔLCR (CDS of
307 NM_001001671.3 with c.1_2,712del, c.3,535_3,675del, c.3,838_3,879del), PBM1
308 (R58A/R59A; CDS of NM_001001671.3 with c.147C>T, c.172CGGCGG>GCCGCC,
309 c.574G>A), PBM2 (R203A/R204A; CDS of NM_001001671.3 with c.147C>T,
310 c.574G>A, c.607AGACGA>GCCGCC), PBM3 (R252A/K253A/R255A; CDS of
311 NM_001001671.3 with c.147C>T, c.574G>A, c.754CGGAAA>GCCGCC,
312 c.763AGA>GCC), PBM4 (R332A/R333A; CDS of NM_001001671.3 with c.147C>T,
313 c.574G>A, c.994AGGAGA>GCCGCC), PBM5 (R391A/K392A; CDS of
314 NM_001001671.3 with c.147C>T, c.574G>A, c.1,171CGCAAA>GCCGCC), PBM6
315 (R424A/K425A; CDS of NM_001001671.3 with c.147C>T, c.574G>A,
316 c.1,270AGGAAA>GCCGCC), PBM7 (R436A/K437A; CDS of NM_001001671.3 with
317 c.147C>T, c.574G>A, c.1,306AGAAAA>GCCGCC), PBM8
318 (R493A/R494A/K496A/K497A; CDS of NM_001001671.3 with c.147C>T, c.574G>A,
319 c.1,477CGGCG>GCCGC, c.1,686AAGAAA>GCCGCC), PBM9 (K797A/R798A; CDS
320 of NM_001001671.3 with c.147C>T, c.574G>A, c.2,389AAACGT>GCCGCC) and
321 PBM10 (K895A/R896A; CDS of NM_001001671.3 with c.147C>T, c.574G>A,
322 c.2,683AAACGT>GCCGCC) were constructed from full-length ASK3 and subcloned
323 into pcDNA4/TO with an N-terminal EGFP-FLAG-tag. CIDRs in ASK3 were predicted
324 using the IUPred2A tool (*46*) (URL https://iupred2a.elte.hu/) (Fig. S2B). PBMs in ASK3
325 were defined based on the central positively charged $[KR]_5$-$[KR]_6$ in the consensus
326 sequence (*38, 39*) (Fig. S5A). The ASK3 PBM4 mutant was also subcloned into
327 pcDNA3/GW with an N-terminal HA-tag or pcDNA3 with a C-terminal tdTomato-tag.
328 The ASK3 CT mutant was also subcloned into pcDNA3 with a C-terminal tdTomato-tag.
329 Human ANKRD52 was cloned previously (*17*) and subcloned into pcDNA3/GW with a
330 C-terminal Venus-tag. Human NAMPT (CDS of NM_005746.2) was cloned from a
331 cDNA pool derived from HEK293A cells and subcloned into pcDNA3/GW with an N-
332 terminal FLAG-tag. NAMPT mutants S199D (CDS of NM_005746.2 with
333 c.595TC>GA) and S200D (CDS of NM_005746.2 with c.598TC>GA) (*29*) were
334 constructed from full-length NAMPT and subcloned into pcDNA3/GW with an N-
335 terminal FLAG-tag. Human PPP6R3 (CDS of NM_001164161.1) with an N-terminal
336 YFP-tag and human PPP6C (CDS of NM_002721.4) with a C-terminal HA-tag were
337 constructed previously (*17*). Human PARG (CDS of NM_001303486.1) and human
338 SIRT2 (CDS of NM_030593.2) were cloned from a cDNA pool derived from HEK293A
339 cells and subcloned into pcDNA3/GW with a C-terminal HA-tag. PARG mutant
340 E673A/E674A (CDS of NM_001303486.1 with c.2,018AAGAA>CCGCC) (*34*) was
341 constructed from full-length PARG and subcloned into pcDNA3/GW with a C-terminal
342 HA-tag. The wild-type PARG and PARG mutant were also subcloned into pcDNA3/GW
343 with a C-terminal Venus-tag. Human PABPC1 (CDS of NM_002568.4) and human
344 DCP1A (CDS of NM_018403.7) were cloned from a cDNA pool derived from
345 HEK293A cells and subcloned into pcDNA3/GW with an N-terminal HA- and Venus-
346 tag, respectively. Human CD38 (CDS of NM_001775.3) was cloned from a cDNA pool
347 derived from A594 cells and subcloned into pcDNA3/GW with a C-terminal HA-tag.
348 Human PARP1 (CDS of NM_001618.3) was cloned from a cDNA pool derived from
349 HeLa cells and subcloned into pcDNA3/GW with an N-terminal HA-tag. WWE domain
350 in human RNF146 (c.247–549 in CDS of NM_030963.3) (*40, 47*) was cloned from a

351 cDNA pool derived from HEK293A cells and subcloned into pcDNA4/TO with an N-
352 terminal EGFP-FLAG-tag. Empty vectors were used as negative controls.
353   Small interfering RNAs (siRNAs) for human *NAMPT* (#1: 5′-
354 CCACCGACUCCUACAAGGUUACUCA-3′, #2: 5′-
355 GAUCUUCUCCAUACUGUCUUCAAGA-3′, #3: 5′-
356 GAAUAUUGAACUGGAAGCAGCACAU-3′) were purchased as Stealth RNAi siRNAs
357 from Invitrogen. The target sequences were designed using the Block-iT RNAi Designer
358 tool (Invitrogen, current URL https://rnaidesigner.thermofisher.com/rnaiexpress/). As the
359 negative control, Stealth RNAi Negative Control Medium GC Duplex #2 (Invitrogen,
360 Cat. #12935-112) was used.
361
362 **Cell culture**
363 HEK293A cells were cultured in Dulbecco's modified Eagle's medium (DMEM)
364 (Sigma-Aldrich, Cat. #D5671) supplemented with 10% fetal bovine serum (FBS;
365 BioWest, Cat. #S1560-500) and 100 units/mL penicillin G (Meiji Seika, Cat.
366 #6111400D2039). Tetracycline-inducible Venus-ASK3-stably expressing HEK293A
367 (Venus-ASK3-HEK293A) cells were established with the T-REx system (Invitrogen).
368 Tetracycline-inducible FLAG-ASK3-stably expressing HEK293A (FLAG-ASK3-
369 HEK293A) cells were established previously (*17*). Venus-ASK3-HEK293A cells and
370 FLAG-ASK3-HEK293A cells were cultured in DMEM supplemented with 10% FBS, 2.5
371 μg/mL blasticidin (Invitrogen, Cat. #A1113903) and 50 μg/mL Zeocin (Invitrogen, Cat.
372 #R25001). To induce Venus-ASK3 or FLAG-ASK3, the cells were pretreated with 1
373 μg/mL tetracycline (Sigma-Aldrich, Cat. #T7660) 24 hr before assays. All cells were
374 cultured in 5% CO_2 at 37ºC and verified to be negative for mycoplasma.
375
376 **Transfections**
377 Plasmid transfections were performed with polyethylenimine "MAX" (Polysciences, Cat.
378 #24765) when HEK293A cells were grown to 95% confluency, according to a previously
379 described protocol (*48*) with minor optimization. To reduce cytotoxicity, the cells were
380 cultured in fresh medium 6–10 hr later, followed by another 40 hr of culture. siRNA
381 transfections for FLAG-ASK3-HEK293A cells were carried out by forward transfection
382 using Lipofectamine RNAiMAX (Invitrogen, Cat. #133778-500) and 10 nM siRNAs
383 once the cells reached 40–80% confluency, according to the manufacturer's instructions.
384 siRNA transfections for HEK293A cells were carried out by reverse transfection using
385 Lipofectamine RNAiMAX and 30 nM siRNAs, according to the manufacturer's
386 instructions.
387
388 **Osmotic stress treatments**
389 In live-cell imaging experiments, osmotic stress was applied by adding the 2x osmotic
390 medium into the culture medium, followed by the incubation in 5% CO_2 at 37ºC. For
391 isoosmotic conditions (~300 mOsm/kg H_2O), DMEM supplemented with 10% FBS was
392 used as the isoosmotic medium. For hyperosmotic stress (~400, ~500, ~600 or ~700
393 mOsm/kg H_2O), DMEM supplemented with 10% FBS and 200, 400, 600 or 800 mM
394 mannitol was used as the 2x hyperosmotic medium. In the case of NaCl-based
395 hyperosmotic stress (~400, ~500 or ~600 mOsm/kg H_2O), DMEM supplemented with
396 10% FBS and 100, 200 or 300 mM NaCl was used as the 2x hyperosmotic medium. For

hypoosmotic stress (~150 or 225 mOsm/kg H_2O), ultrapure water or 2-fold diluted isoosmotic medium was used as the 2x hypoosmotic medium.

In immunoblotting experiments, osmotic stress was applied by exchanging the culture medium with osmotic buffer. The isoosmotic buffer (300 mOsm/kg H_2O, pH 7.4) contained 130 mM NaCl, 2 mM KCl, 1 mM KH_2PO_4, 2 mM $CaCl_2$, 2 mM $MgCl_2$, 10 mM 4-(2-hydroxyethyl)-1-piperazineethanesulfonic acid (HEPES), 10 mM glucose and 20 mM mannitol. The hyperosmotic buffer (425 or 500 mOsm/kg H_2O, pH 7.4) was the same as the isoosmotic buffer but contained 145 or 220 mM mannitol, respectively. Absolute osmolality was verified by an Osmomat 030 (Gonotec) osmometer to fall within the range of 295 to 320 mOsm for isoosmotic buffer or $\pm$ 25 mOsm/kg H_2O for the other buffers.

Live-cell imaging

Cells were seeded in 35 mmφ glass bottom dishes (Matsunami, Cat. #D11130H) coated with 1% gelatin (Nacalai Tesque, Cat. #16605-42) in phosphate-buffered saline (PBS; 137 mM NaCl, 3 mM KCl, 8 mM Na_3PO_4•$12H_2O$, 15 mM KH_2PO_4). For transfected HEK293A cells, the cells were reseeded from a 24-well plate into glass bottom dishes 24 hr after transfection. After 36–60 hr, the culture medium was replaced with 1 mL isoosmotic medium per dish, and the dish was subsequently viewed a TCS SP5 (Leica) confocal laser-scanning microscope equipped with a stage top incubator (Tokai Hit). The cells were observed in 5% CO_2 at 37ºC using an HC PL APO 63x/1.40 oil objective (Leica). Multichannel time-lapse images were acquired in 4 fields each with 4 averages per frame in 1-min or 1.5-min intervals. Venus, EGFP or tdTomato was excited at 514 nm with an argon laser, at 488 nm with an argon laser or at 561 nm with a DPSS laser, respectively, and detected by a HyD detector (Leica). Differential interference contrast (DIC) was captured through the transmitted light from either the argon or DPSS laser, the unused laser in the observation, and detected by a PMT detector (Leica). After obtaining image sets for 5 min under isoosmotic conditions as the "Before" condition, the cells were exposed to osmotic stress by adding 1 mL of 2x osmotic medium per dish and continuously observed for 30 min. Of note, although the cellular morphology was appreciably changed under osmotic stress, we observed the constant position, XY and focal plane, by utilizing a motorized stage and the on-demand mode of adaptive focus control system (Leica) in each field.

In the experiments of the dynamics and fusion of ASK3 condensates, single-channel time-lapse imaging for Venus was performed in a single field with 2 averages per frame at the minimum interval (~1 sec). To hold a constant position and minimize the autofocusing time, the continuous mode of adaptive focus control system was applied. Similarly, the relationship between ANKRD52 and ASK3 condensates was investigated by 2-channel time-lapse imaging for Venus and tdTomato at the minimum interval (~5 sec).

In the experiments of the reversibility of ASK3 condensates, time-lapse images of the EGFP and DIC channels were captured by the following procedure. After acquiring the "Before" image sets for 5 min under isoosmotic conditions, the cells were exposed to hyperosmotic stress (600 mOsm) by adding 1 mL of 2x hyperosmotic medium per dish and observed for 20 min. Subsequently, the cells were reverted back to isoosmotic conditions by adding 2 mL of ultrapure water per dish and further observed for 20 min.

443   For presentation, representative raw images were adjusted in brightness and contrast
444   linearly and equally within the samples by using the GNU Image Manipulation Program
445   (GIMP; GIMP Development Team, URL https://www.gimp.org/) or ImageJ/Fiji (*49*)
446   (URL https://fiji.sc/) software. Because we used DIC images as a rough confirmation of
447   cytosol region, automatically optimized adjustment in brightness and contrast was
448   applied to each DIC image; therefore, the signal intensity of DIC image cannot be
449   compared among the images. To create a time-lapse video, a series of images were
450   equally adjusted in brightness and contrast (and assigned colors if multiple channels were
451   included); captions were added, and the images were converted to a movie file using
452   ImageJ/Fiji software.
453   For quantification, we established a macro script in ImageJ/Fiji to calculate the count
454   and size of ASK3 condensates in a cell per frame and applied it to all raw image sets in
455   batch mode. Briefly, based on a DIC image, the region of interest (ROI) was first defined
456   as the whole cell area of a main cell because there are condensates from another cell in
457   some cases. After applying a Gaussian filter, the Venus signal within the ROI was
458   subsequently extracted from a Venus image in accordance with the local threshold.
459   Finally, particle analysis was performed. Each parameter was determined from pilot
460   analyses in Venus-ASK3-HEK293A cells. The exported data table was summarized with
461   R language on RStudio (RStudio, Inc., URL https://rstudio.com/) software. The
462   ImageJ/Fiji script also exported images of both ROIs and identified particles, enabling us
463   to confirm the quality. In fact, we excluded several data points from the data analysis: (1)
464   if the image was out-of-focus, (2) if the target cell was shrunken too much or detached
465   completely or (3) if the value was an extreme outlier, less than $Q_1 - 5 \times$ IQR or more
466   than $Q_3 + 5 \times$ IQR, where Q_1, Q_3 and IQR are the 1st quartile, the 3rd quartile and the
467   interquartile range, respectively.
468
469   **Fluorescence recovery after photobleaching assay**
470   Ideally, fluorescence recovery after photobleaching (FRAP) should be applied to only a
471   single condensate. However, ASK3 condensates move around too dynamically and
472   rapidly to be evaluated by normal FRAP assay; ASK3 condensates go out from the focal
473   plane and vice versa, for example. Hence, we established and performed a subsequent
474   FRAP assay for ASK3 condensates under hyperosmotic stress. Prior to the FRAP assay,
475   ASK3-tdTomato-transfected HEK293A cells were placed under the microscope in 5%
476   CO_2 at 37ºC and exposed to hyperosmotic stress (600 mOsm) for 30 min, which makes
477   ASK3 condensates relatively stable. Subsequently, single-channel time-lapse imaging for
478   tdTomato was performed in a single field with 4 averages per frame with a minimum
479   interval (~2.1 sec) by utilizing the continuous mode of adaptive focus control system.
480   After acquiring 5 frame as the "Before" condition, a rectangular area that included more
481   than 10 condensates (with the exception of the ASK3 CT mutant for which 1 condensate
482   was included) was photobleached by the maximum intensity of the DPSS laser three
483   times, followed by the time-lapse imaging of 100 intervals as the "After" condition.
484   To quantify the FRAP rate of ASK3 condensates from image data, particle tracking
485   analysis was first executed for all ASK3 condensates by using a Fiji plugin TrackMate
486   (*50*) (URL https://imagej.net/TrackMate). In TrackMate, each condensate was identified
487   in each frame by a Laplacian of Gaussian (LoG) detector, followed by connecting frames
488   by a linear assignment problem (LAP) tracker. Each parameter was determined from pilot

489   analyses for ASK3(WT)-tdTomato. In this tracking analysis, we excluded the
490   condensates (1) that were not successfully tracked from "Before" to "After" or (2) that
491   were present in less than 25 frames. Next, the tracking data table was used to
492   systematically calculated to the FRAP rate in RStudio software. In the R script, each
493   tracked condensate was first categorized into 2 groups, photobleached or not-
494   photobleached, based on the XY coordinates of the photobleached rectangular area.
495   Meanwhile, the fluorescence intensity value of condensate i at time t, $F_i(t)$ was converted
496   to the relative fluorescence change $F_i(t) / F_{i,\text{Before}}$, where $F_{i,\text{Before}}$ indicates the mean of
497    $F_i(t)$ for each condensate i in the "Before" condition. At this step, we eliminated a few
498   false positive condensates in the photobleached group whose $F_i(t) / F_{i,\text{Before}}$ did not exhibit
499   at least a 15% decrease between the "Before" and "After" conditions, although $F_i(t) /$
500    $F_{i,\text{Before}}$ of the other photobleached condensates dropped by an average of 80% in our
501   FRAP assays. To correct the quenching effects during observation, each $F_i(t) / F_{i,\text{Before}}$ in
502   the photobleached group was normalized to $G_i(t) = (F_i(t) / F_{i,\text{Before}}) / $ (the mean of $F_j(t) /$
503    $F_{j,\text{Before}}$ in the nonphotobleached group). To mitigate the effects of condensate movement
504   in a direction vertical to the focal plane on the changes in fluorescence, $G_i(t)$ was further
505   converted to the mean of $G_i(t)$ in the photobleached group, $G(t)$; namely, we summarized
506   all values of the photobleached condensates in a cell into representative values of one
507   virtual condensate. Finally, the FRAP rate [%] at time t in the cell was calculated as $(G(t)$
508    $- G_{\text{Min}}) / (1 - G_{\text{Min}}) \times 100$, where G_{Min} was the minimum value within the first three time
509   points of the "After" condition. When summarizing the FRAP rate between cells, we
510   trimmed a few extreme outliers, less than $Q_1 - 5 \times \text{IQR}$ or more than $Q_3 + 5 \times \text{IQR}$.
511

512   **Immunocytochemistry and immunofluorescence**
513   Transfected HEK293A cells were seeded on 15 mmφ cover slips (Matsunami, Cat.
514   #C015001) coated with 1% gelatin in PBS in a 12-well plate. After 24–48 hr, the cells
515   were exposed to osmotic medium or buffer for the indicated period, followed by the
516   following immunostaining steps: fixation for 15 min with 4% formaldehyde (Wako Pure
517   Chemical Industries, Cat. #064-00406) in PBS, permeabilization for 15 min with 1%
518   Triton X-100 (Sigma, Cat. #T9284) in PBS, blocking for 30 min with 5% skim milk
519   (Megmilk Snow Brand) in TBS-T (50 mM tris(hydroxymethyl)aminomethane (Tris)-HCl
520   pH 8.0, 150 mM NaCl and 0.05% Tween 20) and incubation at 4ºC overnight with the
521   primary antibodies in 1st antibody dilution buffer (TBS-T supplemented with 5% bovine
522   serum albumin (BSA; Iwai Chemicals, Cat. #A001) and 0.1% NaN_3 (Nacalai Tesque,
523   Cat. #312-33)). The cells were further incubated at room temperature in the dark for 1–2
524   hr with the appropriate fluorophore-conjugated secondary antibodies in TBS-T. After
525   counterstaining with Hoechst 33258 dye (Dojindo, Cat. #343-07961, 1:2,000) in TBS-T
526   for 5 min, the cover slips were mounted on glass slides with Fluoromount/Plus
527   (Diagnostic Biosystems, Cat. #K048). The samples were observed by using an LSM 510
528   META (Zeiss) or a TCS SP5 microscope with the 63x/1.40 oil objective. To distinguish
529   the background fluorescence or the "bleed-through" of the other fluorophore from the
530   true signal, we also confirmed the proper negative control samples in each observation.
531

532   **Immunoelectron microscopy using ultrathin cryosections**
533   After Venus-ASK3-HEK293A cells were exposed to hyperosmotic stress (800 mOsm, 3
534   hr), the cells were fixed at room temperature for 10 min with 4% paraformaldehyde

(PFA) in 0.1 M phosphate buffer (pH7.2) (PB), followed by the replacement with fresh 4% PFA in PB and incubation at 4ºC overnight. Cells were washed 3 times with PBS, followed by 0.15% glycine in PBS, and embedded in 12% gelatin in 0.1 M PB. Small blocks were rotated in 2.3 M sucrose in PB at 4ºC overnight and quickly plunged into liquid nitrogen. Sections approximately 60 nm thick were cut using a UC7/FC7 ultramicrotome (Leica) and picked up with a 1:1 mixture of 2% methylcellulose and 2.3 M sucrose in PB. The sections were incubated at 4ºC overnight with rabbit anti-GFP antibody (Frontier Institute, Ishikari, Japan, Cat. GFP-Rb-Af2020), followed by incubation at room temperature for 1 hr with protein A conjugated to 10-nm gold particles (protein A-gold; Cell Microscopy Center, University Medical Center Utrecht, Utrecht, the Netherlands). The sections were embedded in a thin layer of 2% methylcellulose with 0.4% uranyl acetate (pH 4.0) and observed with a H-7100 (Hitachi) transmission electron microscope. For control experiments, ultrathin sections were reacted only with protein A-gold.

In vitro condensation assay

For protein purification, HEK293A cells were seeded in 10 cmφ dishes and transfected with EGFP-FLAG-tagged constructs. After washing with PBS, the cells were lysed in lysis buffer (20 mM Tris-HCl pH 7.5, 150 mM NaCl, 5 mM ethylene glycol-bis(2-aminoethylether)-N,N,N',N'-tetraacetic acid (EGTA), 1% sodium deoxycholate, 1% Triton X-100 and 12 mM β-glycerophosphatase) supplemented with protease inhibitors (1 mM phenylmethylsulfonyl fluoride (PMSF) and 5 μg/mL leupeptin), phosphatase inhibitor cocktail I (8 mM NaF, 1 mM Na_3VO_4, 1.2 mM Na_2MoO_4, 5 μM cantharidin and 2 mM imidazole) and 1 mM dithiothreitol (DTT). The cell extracts were collected with a scraper from 3 dishes into a single microtube for each protein, followed by centrifugation at 4ºC and 13,500 rpm (~16,500 × g) for 15 min. The supernatants were incubated with anti-FLAG antibody beads (Sigma-Aldrich, clone M2, Cat. #A2220) at 4ºC for ~3 hr. The beads were washed 4 times with wash buffer (20 mM Tris-HCl pH 7.5, 500 mM NaCl, 5 mM EGTA, 1% Triton X-100 and 2 mM DTT) and once with TBS (20 mM Tris-HCl pH 7.5, 150 mM NaCl and 1 mM DTT). The EGFP-FLAG-tagged proteins were eluted from the beads with 0.1 mg/mL 3x FLAG peptide (Sigma-Aldrich, Cat. #F4799) in TBS at 4ºC for more than 1 hr, followed by dilution to 40 μM with TBS. The concentration of the protein was estimated from the absorbance at 280 nm measured by a SimpliNano (GE healthcare) microvolume spectrophotometer with the extinction coefficient calculated by using the ExPASy ProtParam tool (*51*) (https://web.expasy.org/protparam/).

The purified EGFP-FLAG-tagged protein was diluted into a sample in a microtube, whose control conditions were 10 μM EGFP-FLAG-tagged protein, 150 mM NaCl, 20 mM Tris (pH 7.5), and 1 mM DTT. When increasing the macromolecular crowding, Ficoll PM400 (GE Healthcare, Cat. #17-0310-10) or polyethylene glycol 4000 (PEG; Kanto Kagaku, Cat. #32828-02) was included in the sample at the indicated concentration. When modifying the ion strength and concentration, the concentration of NaCl was changed as indicated. When investigating the effects of poly(ADP-ribose) (PAR) on ASK3 condensates, 20% PEG was added as a crowding reagent, and the indicated concentration of PAR polymer (Trevigen, Cat. #4336-100-01) or β-nicotinamide adenine dinucleotide (NAD; Sigma-Aldrich, Cat. #N7004) in TE (10 mM

581   Tris-HCl pH 8.0 and 1 mM ethylenediaminetetraacetic acid (EDTA)) was also added.
582   The prepared sample was subsequently incubated at 4ºC for 15 min. The reaction mixture
583   was immediately loaded into a counting chamber with a cover slip (Matsunami, Cat. #
584   C018241), followed by observation using a TCS SP5 microscope with a 63x/1.40 oil
585   objective. To maintain a constant focal plane even if there were no condensates, we set
586   the focal plane adjacent to the surface of the cover slip by utilizing the motorized stage
587   and the on-demand mode of adaptive focus control system. Images of the EGFP signal
588   were captured from 5 random fields per sample. The above protein purification
589   procedures were performed in each independent experiment. Of note, when we
590   photobleached the fluorescence of ASK3 condensates, we could not observe FRAP;
591   therefore, the condensates produced by our in vitro assays are solid-like, possibly because
592   the maturation of ASK3 condensation occurs too fast in vitro.

593   For presentation, representative raw images were adjusted in brightness and contrast
594   linearly and equally within the samples using ImageJ/Fiji software. For quantification, we
595   established a macro script in ImageJ/Fiji to calculate the fluorescent intensity and area of
596   ASK3 condensates in each sample and applied the script to all raw image sets in batch
597   mode. In the script, a Gaussian filter and background correction were applied to each
598   image, followed by particle analysis. Each parameter was determined from pilot analyses
599   for EGFP-FLAG-ASK3 WT. The exported data table was further summarized in RStudio
600   software. In the R script, the amount of ASK3 condensates in a sample was defined as the
601   mean of total intensity within 5 fields. When investigating the effects of PAR, the amount
602   value was divided by the amount of the internal standard sample, i.e., the control sample
603   without TE addition. When comparing the effects of PAR between ASK3 mutants, the
604   amount value was converted to the amount relative to the mean of the control sample
605   between experiments.

606
607   **Immunoblotting**
608   Cells were lysed in lysis buffer (20 mM Tris-HCl pH 7.5, 150 mM NaCl, 10 mM EDTA,
609   1% sodium deoxycholate, and 1% Triton X-100) supplemented with protease inhibitors
610   (1 mM PMSF and 5 μg/mL leupeptin). When detecting the phosphorylation of
611   endogenous proteins, phosphatase inhibitor cocktail II (20 mM NaF, 30 mM β-
612   glycerophosphatase, 2.5 mM Na_3VO_4, 3 mM Na_2MoO_4, 12.5 μM cantharidin and 5 mM
613   imidazole) was also supplemented. When detecting the PARsylated proteins, 1 mM
614   nicotinamide (Sigma-Aldrich, Cat. #N0078) and 100 μM gallotanin (Sigma-Aldrich, Cat.
615   #403040) were also supplemented as PARP and PARG inhibitors, respectively. Cell
616   extracts were clarified by centrifugation at 4ºC and 13,500 rpm (~16,500 × g) for 15 min,
617   and the supernatants were sampled by adding 2x sample buffer (80 mM Tris-HCl pH 8.8,
618   80 μg/mL bromophenol blue, 28.8% glycerol, 4% sodium dodecyl sulfate (SDS) and 10
619   mM DTT). After boiling at 98ºC for 3 min, the samples were resolved by SDS-PAGE
620   and electroblotted onto a BioTrace PVDF (Pall), FluoroTrans W (Pall) or Immobilon-P
621   (Millipore, Cat. #IPVH00010) membrane. The membranes were blocked with 2.5% or
622   5% skim milk in TBS-T and probed with the appropriate primary antibodies diluted by
623   the 1st antibody dilution buffer. After replacing and probing the appropriate secondary
624   antibodies diluted with skim milk in TBS-T, antibody-antigen complexes were detected
625   on X-ray films (FUJIFILM, Cat. #47410-07523, #47410-26615 or #47410-07595) using

626   an enhanced chemiluminescence system (GE Healthcare). The films were converted to
627   digital images by using a conventional scanner without any adjustment.
628   For presentation, representative images were acquired by linearly adjusting the
629   brightness and contrast using GIMP software. When digitally trimming superfluous lanes
630   from blot images, the procedure was executed after the adjustment, and the trimming was
631   clearly indicated. Quantification was performed against the raw digital images with
632   densitometry using Fiji/ImageJ software (*17*). "Kinase activity", "Interaction" and
633   "PARsylated proteins" were defined as the band intensity ratio of phosphorylated protein
634   to total protein, the band intensity ratio of coimmunoprecipated protein to input protein
635   and the band intensity ratio of PARsylated proteins to actin, respectively. For the kinase
636   activity of endogenous ASK3, the ratio of phosphorylated ASK to ASK3 was calculated.
637
638   **Coimmunoprecipitation assay**
639   The supernatants of cell extracts were incubated with anti-FLAG antibody beads (Wako
640   Pure Chemicals Industries, clone 1E6, Cat. #016-22784) for 30–120 min at 4ºC. The
641   beads were washed twice with wash buffer (20 mM Tris-HCl pH 7.5, 500 mM NaCl, 1%
642   sodium deoxycholate, 1% Triton X-100, 0.2% SDS) and once with lysis buffer, followed
643   by the direct addition of 2x sample buffer.
644
645   **Computational model and simulation**
646   To understand the essential principles of ASK3 condensation in a cell under
647   hyperosmotic stress, we utilized and developed the previously reported simple
648   computational model (*18*) with the effects of macromolecule crowding (Fig. S1G).
649   According to the previous model, each single unit of self-associating ASK3 protein is
650   regarded as an even square that occupies a lattice in a two-dimensional grid space
651   corresponding to a single cell. When an ASK3 unit is adjacent to another, the ASK3 units
652   have a binding relationship, which is independent of other binding pairs. Each ASK3 unit
653   has no relationship between nonadjacent ASK3. A cluster of consecutive multiple ASK3
654   units is considered as a condensate in cells, which can be assumed to be a liquid-like or
655   solid-like condensate depending on the system parameters mentioned below. At each
656   time step, an ASK3 unit can move to an adjacent lattice. Given the original position of
657   the ASK3 unit, this movement is categorized into three physicochemical actions: (1)
658   diffusion, (2) exchange/vibration and (3) unbinding. If there are no neighboring ASK3
659   units before the movement (the destination 1 in Fig. S1G), the movement is considered
660   simple diffusion with the rate constant k_1. If there is more than one neighboring ASK3
661   unit before the movement and if the destination position is already occupied by one of the
662   neighbors (the destination 2 in Fig. S1G), the movement corresponds to an exchange
663   between the ASK3 units in a cluster, namely, a rearrangement process within a liquid-like
664   condensate. This exchange action is obeyed by the rate constant k_2. When k_2 is small, the
665   action is considered vibration of ASK3 in a solid-like condensate. If there is more than
666   one neighboring ASK3 units before the movement and if the destination position is
667   occupied by none of the neighbors (the destination 3a–c in Fig. S1G), the movement can
668   be accompanied by breakages of the binding relationships with the neighbors, i.e., the
669   unbinding reaction. According to the simple Arrhenius equation, a rate constant of this
670   overall unbinding movement k_3 is defined as $k_3 = A \times \exp(-\Delta E \times n_{\text{lost}} / \theta)$, where A is a
671   frequency factor, ΔE is an activation energy in the unbinding reaction between a single

672　pair of ASK3 units, n_{lost} is the number of neighboring ASK3 units whose binding
673　relationship with the ASK3 unit to move will be lost by the movement, and θ is a
674　temperature-like constant. Notably, the unbinding movement of ASK3 unit includes not
675　only the dissociation process from the condensate but also the rearrangement process of
676　the condensate (compare the destination 3a with the destinations 3b and 3c in Fig. S1G).
677　Moreover, due to the penalty factor n_{lost}, the rearrangement that increases the surface of
678　condensate (regarded as blue-colored positions in Fig. S1G for the clusters of 2 ASK3
679　units, for example) is less likely than the rearrangement that maintains in most cases
680　(consider all potential patterns of the case when the destination 4b in Fig. S1G is
681　occupied by not obstacle but ASK3 unit, for example). When $n_{lost} = 0$ (the destination 3c
682　in Fig. S1G), that is, $k_3 = A$, the unbinding movement is considered a shape-modified
683　rearrangement process of the condensate with a void unbinding reaction. In our model,
684　obstacles were further added to reflect on the effects of macromolecular crowding in a
685　cell. Each obstacle basically has the same properties as ASK3 unit; the obstacles takes the
686　same size and shape as ASK3 unit, occupies a grid element and can move to an adjoining
687　position. However, each obstacle has neither a binding relationship with ASK3 units nor
688　one with the other obstacles, that is, each obstacle has neither a positive nor a negative
689　effect on the other molecules. Hence, in addition to the above three physicochemical
690　actions of an ASK3 unit, a new action arises: (4) reflection. If the destination position is
691　occupied by an obstacle (the destination 4a and 4b in Fig. S1G), the ASK3 unit is not
692　able to move to the destination; therefore, the ASK3 unit is reflected by the obstacle and
693　"moves to" the original position according to the rate constant k_4. Simultaneously, the
694　movement of an obstacle is categorized into three physicochemical actions: (5) diffusion,
695　(6) reflection by an ASK3 unit and (7) reflection by an obstacle. If the destination
696　position is unoccupied (the destination 5 in Fig. S1G), the movement is simple diffusion
697　of the obstacle according to the rate constant k_5. If the destination position is already
698　occupied by an ASK3 unit or another obstacle (the destination 6 or 7 in Fig. S1G), the
699　movement corresponds to reflection by the ASK3 unit or the other obstacle, and the
700　obstacle "moves to" the original position depending on the rate constant k_6 or k_7,
701　respectively. We note that the ASK3 unit in our model may not necessarily correspond to
702　a monomer of a single ASK3 peptide in the real world but homo-oligomer(s) of ASK3 or
703　even hetero-oligomer(s). Likewise, the obstacle unit in our model is a virtual molecule
704　that corresponds to the integration of subcellular molecules in the real world, such as
705　macromolecules, small molecules and ions.
706　　　　To simulate with the model in silico, we computed random trajectories of both ASK3
707　units and obstacles using the rejection kinetic Monte Carlo (rKMC) method in Python
708　language. Briefly, the Phyton script executed the following algorithm. First, all ASK3
709　units and obstacles were randomly located in the grid space as an initial condition. Next,
710　a target molecule with a chance to move was randomly picked from the union of the
711　ASK3 unit and obstacle populations, followed by the random selection of a potential
712　destination position of the selected target. As mentioned in the above model description,
713　the designation of the target and destination systematically assigned k, the rate constant of
714　the potential movement. At the same time, a random number r was acquired from the
715　interval [0, 1). If $k \geq r$, the movement was accepted, and the target was renewed at the
716　position of the destination, although the target was "renewed" at the original position in
717　cases of reflection. Otherwise, if $k < r$, the movement was denied, and the target stayed at

718   the original position. After this determination, the iteration step number was incremented
719   by one, and the next iteration step began by randomly selecting the next target molecule.
720   In the simulation, we regarded k_4, k_6 and k_7 as dummy constants, and we ignored their
721   calculations for the reflection processes because the target molecule remained at its
722   original position in all cases. Since the goal of the computational simulation in this study
723   was not to understand the phase of condensates but to understand the driving force of
724   ASK3 condensation, we also regarded k_2 as a dummy constant and ignored its calculation
725   for the exchange/vibration process. We set $k_1 = 1$; therefore, free diffusion of ASK3 was
726   always accepted. In contrast, we set $k_5 = 0.01$; therefore, the diffusion of an obstacle was
727   slower than diffusion of ASK3 unit. This assumption is not unusual because each
728   virtually integrated obstacle is considered the average movement of the constituent
729   molecules, whose movement vectors mostly cancel each other out. For the critical
730   penalty-defining constant k_3, we set $A = 1$ to adjust $k_3 = 1$ under the condition where n_{lost}
731    $= 0$ and fixed $\Delta E / \theta = 1$ for simplicity; hence, the maximum speed of ASK3 for moving
732   within the condensate was identical to $k_1 (= 1)$, the free diffusion of ASK3 out of
733   condensate. Of note, the sampling distribution of k_3 in our simulation well satisfied
734   exponential decay curve, that is, rejection sampling was confirmed. We prepared 500
735   ASK3 units with or without 1,500 obstacle units in the grid space. To create the condition
736   under osmotic stress, we changed only the grid space, ranging from 50×50 to 120×120
737   squares.
738   For figure presentation, our Python script saved the coordinates of each molecules,
739   which was rendered using RStudio software. For movie presentation, our Python script
740   also saved representative images at every 10,000 or 100,000 iteration steps, defined as the
741   unit of time t. To make a time-lapse video, a series of images with added captions were
742   converted to a movie file using ImageJ/Fiji software. For quantification, our Python script
743   also calculated the count and size of the ASK3 clusters at every iteration step. To mimic
744   confocal microscopy observations, a cluster of condensates was defined as a cluster of ≥ 6
745   consecutive ASK3 units. The exported data table was summarized in RStudio software.
746
747   **Data analysis and statistical analysis**
748   The data are summarized as the mean ± SEM with the exception of boxplots. No
749   statistical method was utilized to predetermine the sample size. Based on the small
750   sample size and the quality-oriented immunoblotting assays, homoscedasticity was
751   assumed unless $P < 0.01$ in an F-test or Levene's test based on the absolute deviations
752   from the median. Statistical tests, the number of samples and the sample sizes are
753   indicated in Table S2. Statistical tests were performed using R with RStudio software,
754   and $P < 0.05$ was considered statistically significant. In several experiments, a few
755   samples were excluded because they satisfied the criteria clearly outlined in the above
756   sections. The investigators were not blinded to allocation during experiments and
757   outcome assessments. The experiments were not randomized. However, the experiments
758   were performed across different passages of cells, and the cells in the control and treated
759   groups were seeded from the same population of cells.
760
761   **Data availability**
762   Almost all data are included in the main text or the supplementary materials. Further
763   information and requests for resources and reagents should be directed to K.W. and H.I.

764
765 **Supplementary Materials**
766   • Supplementary Text
767   • Fig. S1. Characteristics of ASK3 condensates.
768   • Fig. S2. CCC and CLCR of ASK3 are critical for the ability of ASK3 to condense.
769   • Fig. S3. Quantification of immunoblotting data in main figures.
770   • Fig. S4. Major NAD-consuming enzymes suppress ASK3 activity under hyperosmotic
771   stress.
772   • Fig. S5. ASK3 mutants of PAR-binding motif candidates.
773   • Table S1. List of key resources.
774   • Table S2. Summary of statistical analysis.
775   • Movie S1. A computational simulation for the relationship between the grid space and
776   the number/size of ASK3 clusters.
777   • Movie S2. Dynamics and fusion of ASK3 condensates in Venus-ASK3-stably
778   expressing HEK293A cells.
779   • Movie S3. A computational prediction for ASK3 cluster disassembly after the grid
780   space expansion.
781   • Movie S4. Relationship between ANKRD52 and ASK3 condensates in HEK293A cells.
782
783 **References and Notes**

784 1.   M. L. McManus, K. B. Churchwell, K. Strange, Regulation of cell volume in health and
785   disease. *N. Engl. J. Med.* **333**, 1260–6 (1995).
786 2.   R. L. Rungta *et al.*, The cellular mechanisms of neuronal swelling underlying cytotoxic
787   edema. *Cell.* **161**, 610–621 (2015).
788 3.   V. Compan *et al.*, Cell volume regulation modulates NLRP3 inflammasome activation.
789   *Immunity.* **37**, 487–500 (2012).
790 4.   J. Jantsch *et al.*, Cutaneous Na+ storage strengthens the antimicrobial barrier function of
791   the skin and boosts macrophage-driven host defense. *Cell Metab.* **21**, 493–501 (2015).
792 5.   L. S. King, D. Kozono, P. Agre, From structure to disease: the evolving tale of aquaporin
793   biology. *Nat. Rev. Mol. Cell Biol.* **5**, 687–698 (2004).
794 6.   L. Hooper, D. Bunn, F. O. Jimoh, S. J. Fairweather-Tait, Water-loss dehydration and
795   aging. *Mech. Ageing Dev.* **136–137**, 50–58 (2014).
796 7.   M. D. Allen, D. A. Springer, M. B. Burg, M. Boehm, N. I. Dmitrieva, Suboptimal
797   hydration remodels metabolism, promotes degenerative diseases, and shortens life. *JCI
798   Insight.* **4** (2019), doi:10.1172/jci.insight.130949.
799 8.   F. Lang *et al.*, Functional significance of cell volume regulatory mechanisms. *Physiol.
800   Rev.* **78**, 247–306 (1998).
801 9.   E. K. Hoffmann, I. H. Lambert, S. F. Pedersen, Physiology of cell volume regulation in
802   vertebrates. *Physiol. Rev.* **89**, 193–277 (2009).
803 10.   T. J. Jentsch, VRACs and other ion channels and transporters in the regulation of cell
804   volume and beyond. *Nat. Rev. Mol. Cell Biol.* **17**, 293–307 (2016).
805 11.   J. M. Wood, Osmosensing by bacteria. *Sci. STKE.* **2006**, pe43 (2006).
806 12.   K. Tatebayashi *et al.*, Transmembrane mucins Hkr1 and Msb2 are putative osmosensors in
807   the SHO1 branch of yeast HOG pathway. *EMBO J.* **26**, 3521–33 (2007).
808 13.   F. Yuan *et al.*, OSCA1 mediates osmotic-stress-evoked Ca 2+ increases vital for
809   osmosensing in Arabidopsis. *Nature.* **514**, 367–371 (2014).

810 14. W. Liedtke *et al.*, Vanilloid receptor-related osmotically activated channel (VR-OAC), a
811   candidate vertebrate osmoreceptor. *Cell*. **103**, 525–35 (2000).
812 15. R. Strotmann, C. Harteneck, K. Nunnenmacher, G. Schultz, T. D. Plant, OTRPC4, a
813   nonselective cation channel that confers sensitivity to extracellular osmolarity. *Nat. Cell*
814   *Biol.* **2**, 695–702 (2000).
815 16. I. Naguro *et al.*, ASK3 responds to osmotic stress and regulates blood pressure by
816   suppressing WNK1-SPAK/OSR1 signaling in the kidney. *Nat. Commun.* **3**, 1285 (2012).
817 17. K. Watanabe, T. Umeda, K. Niwa, I. Naguro, H. Ichijo, A PP6-ASK3 Module
818   Coordinates the Bidirectional Cell Volume Regulation under Osmotic Stress. *Cell Rep.* **22**,
819   2809–2817 (2018).
820 18. E. Dine, A. A. Gil, G. Uribe, C. P. Brangwynne, J. E. Toettcher, Protein Phase Separation
821   Provides Long-Term Memory of Transient Spatial Stimuli. *Cell Syst.* **6**, 655-663.e5
822   (2018).
823 19. A. P. Minton, How can biochemical reactions within cells differ from those in test tubes?
824   *J. Cell Sci.* **119**, 2863–2869 (2006).
825 20. N. L. Kedersha, M. Gupta, W. Li, I. Miller, P. Anderson, RNA-binding proteins TIA-1
826   and TIAR link the phosphorylation of eIF-2 alpha to the assembly of mammalian stress
827   granules. *J. Cell Biol.* **147**, 1431–42 (1999).
828 21. J. R. Buchan, R. Parker, Eukaryotic Stress Granules: The Ins and Outs of Translation.
829   *Mol. Cell*. **36**, 932–941 (2009).
830 22. S. F. Banani, H. O. Lee, A. A. Hyman, M. K. Rosen, Biomolecular condensates:
831   Organizers of cellular biochemistry. *Nat. Rev. Mol. Cell Biol.* **18**, 285–298 (2017).
832 23. Y. Shin, C. P. Brangwynne, Liquid phase condensation in cell physiology and disease.
833   *Science (80-.)*. **357**, eaaf4382 (2017).
834 24. S. Boeynaems *et al.*, Protein Phase Separation: A New Phase in Cell Biology. *Trends Cell*
835   *Biol.* **28**, 420–435 (2018).
836 25. S. J. Trevelyan *et al.*, Structure-based mechanism of preferential complex formation by
837   apoptosis signal–regulating kinases. *Sci. Signal.* **13**, eaay6318 (2020).
838 26. B. Stefansson, T. Ohama, A. E. Daugherty, D. L. Brautigan, Protein phosphatase 6
839   regulatory subunits composed of ankyrin repeat domains. *Biochemistry*. **47**, 1442–1451
840   (2008).
841 27. J. R. Revollo, A. A. Grimm, S. I. Imai, The NAD biosynthesis pathway mediated by
842   nicotinamide phosphoribosyltransferase regulates Sir2 activity in mammalian cells. *J.*
843   *Biol. Chem.* **279**, 50754–50763 (2004).
844 28. T. Wang *et al.*, Structure of Nampt/PBEF/visfatin, a mammalian NAD+ biosynthetic
845   enzyme. *Nat. Struct. Mol. Biol.* **13**, 661–2 (2006).
846 29. J. R. Revollo *et al.*, Nampt/PBEF/Visfatin regulates insulin secretion in beta cells as a
847   systemic NAD biosynthetic enzyme. *Cell Metab.* **6**, 363–75 (2007).
848 30. M. Hasmann, I. Schemainda, FK866, a Highly Specific Noncompetitive Inhibitor of
849   Nicotinamide Phosphoribosyltransferase, Represents a Novel Mechanism for Induction of
850   Tumor Cell Apoptosis. *Cancer Res.* **63**, 7436–7442 (2003).
851 31. S. ichiro Imai, L. Guarente, NAD+ and sirtuins in aging and disease. *Trends Cell Biol.* **24**,
852   464–471 (2014).
853 32. W. L. Kraus, PARPs and ADP-Ribosylation: 50 Years . . . and Counting. *Mol. Cell*. **58**,
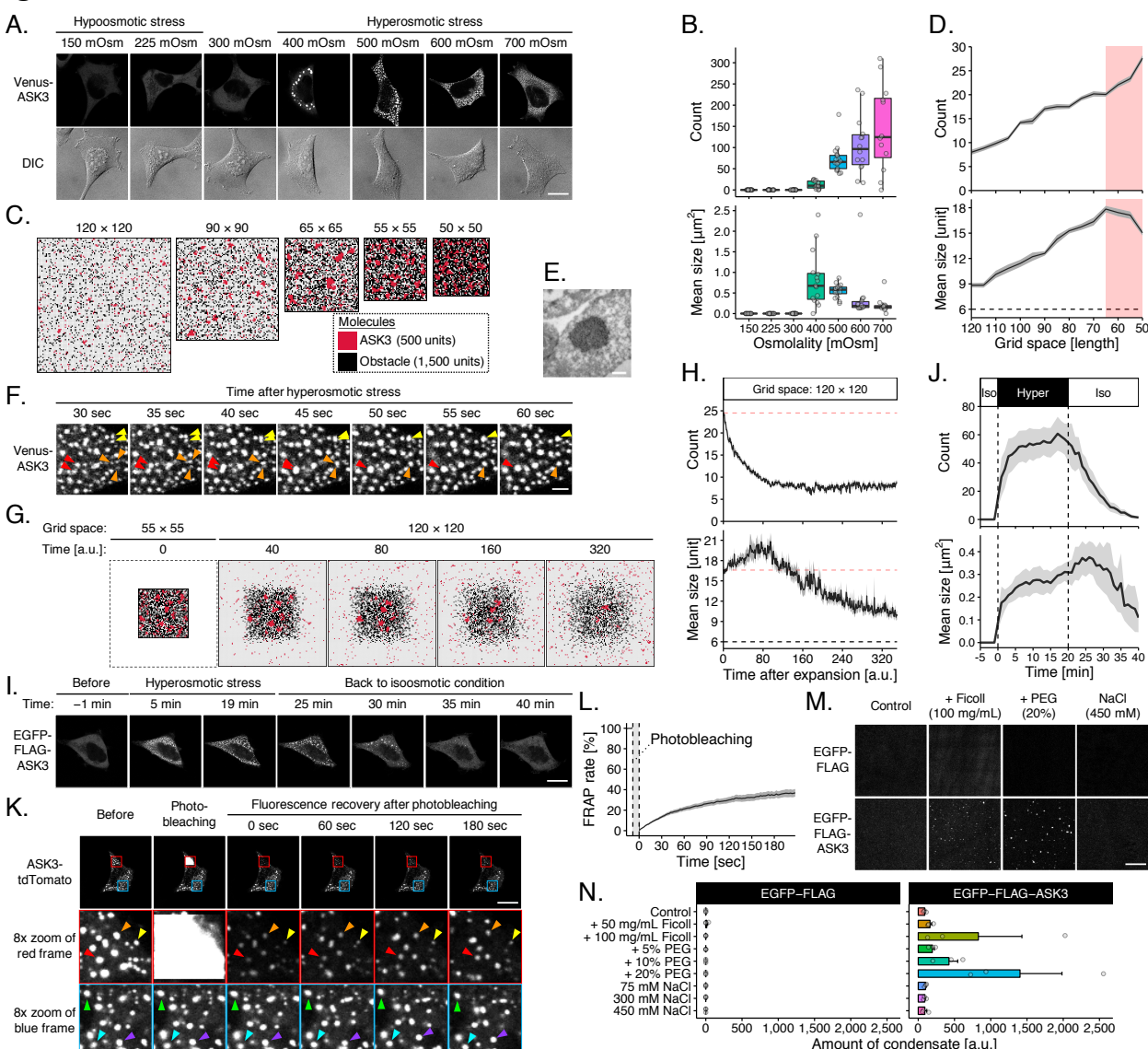854   902–910 (2015).

855 33. E. Barkauskaite, G. Jankevicius, I. Ahel, Structures and Mechanisms of Enzymes
856   Employed in the Synthesis and Degradation of PARP-Dependent Protein ADP-
857   Ribosylation. *Mol. Cell*. **58**, 935–946 (2015).

858 34. N. Le May *et al.*, Poly (ADP-Ribose) Glycohydrolase Regulates Retinoic Acid Receptor-
859   Mediated Gene Expression. *Mol. Cell*. **48**, 785–798 (2012).

860 35. A. K. L. Leung, Poly(ADP-ribose): An organizer of cellular architecture. *J. Cell Biol.* **205**,
861   613–619 (2014).

862 36. A. Patel *et al.*, A Liquid-to-Solid Phase Transition of the ALS Protein FUS Accelerated by
863   Disease Mutation. *Cell*. **162**, 1066–1077 (2015).

864 37. M. Altmeyer *et al.*, Liquid demixing of intrinsically disordered proteins is seeded by
865   poly(ADP-ribose). *Nat. Commun.* **6**, 8088 (2015).

866 38. L. McGurk *et al.*, Poly(ADP-Ribose) Prevents Pathological Phase Separation of TDP-43
867   by Promoting Liquid Demixing and Stress Granule Localization. *Mol. Cell*. **71**, 703-
868   717.e9 (2018).

869 39. J.-P. Gagné *et al.*, Proteome-wide identification of poly(ADP-ribose) binding proteins and
870   poly(ADP-ribose)-associated protein complexes. *Nucleic Acids Res.* **36**, 6959–76 (2008).

871 40. Z. Wang *et al.*, Recognition of the iso-ADP-ribose moiety in poly(ADP-ribose) by WWE
872   domains suggests a general mechanism for poly (ADP-ribosyl)ation-dependent
873   ubiquitination. *Genes Dev.* **26**, 235–240 (2012).

874 41. S. B. Zimmerman, B. Harrison, Macromolecular crowding increases binding of DNA
875   polymerase to DNA: An adaptive effect. *Proc. Natl. Acad. Sci. U. S. A.* **84**, 1871–1875
876   (1987).

877 42. H. B. Schmidt, D. Görlich, Transport Selectivity of Nuclear Pores, Phase Separation, and
878   Membraneless Organelles. *Trends Biochem. Sci.* **41**, 46–61 (2016).

879 43. J. A. Riback *et al.*, Stress-Triggered Phase Separation Is an Adaptive, Evolutionarily
880   Tuned Response. *Cell*. **168**, 1028-1040.e19 (2017).

881 44. D. Bracha *et al.*, Mapping Local and Global Liquid Phase Behavior in Living Cells Using
882   Photo-Oligomerizable Seeds. *Cell*, 1467–1480 (2018).

883 45. S. Maharana *et al.*, RNA buffers the phase separation behavior of prion-like RNA binding
884   proteins. *Science*. **360**, 918–921 (2018).

885 46. B. Mészáros, G. Erdos, Z. Dosztányi, IUPred2A: context-dependent prediction of protein
886   disorder as a function of redox state and protein binding. *Nucleic Acids Res.* **46**, W329–
887   W337 (2018).

888 47. P. A. DaRosa *et al.*, Allosteric activation of the RNF146 ubiquitin ligase by a poly(ADP-
889   ribosyl)ation signal. *Nature*. **517**, 223–226 (2014).

890 48. P. A. Longo, J. M. Kavran, M.-S. Kim, D. J. Leahy, Transient mammalian cell
891   transfection with polyethylenimine (PEI). *Methods Enzymol.* **529**, 227–40 (2013).

892 49. J. Schindelin *et al.*, Fiji: an open-source platform for biological-image analysis. *Nat.*
893   *Methods*. **9**, 676–82 (2012).

894 50. J.-Y. Tinevez *et al.*, TrackMate: An open and extensible platform for single-particle
895   tracking. *Methods*. **115**, 80–90 (2017).

896 51. E. Gasteiger *et al.*, in *The Proteomics Protocols Handbook* (Humana Press, Totowa, NJ,
897   2005; http://link.springer.com/10.1385/1-59259-890-0:571), pp. 571–607.

898

Acknowledgments

Figures and Tables

Fig. 1. ASK3 forms liquid-demixing condensates under hyperosmotic stress. (**A** and **B**) Subcellular localization of ASK3 5 min after osmotic stress in Venus-ASK3-stably expressing HEK293A (Venus-ASK3-HEK293A) cells. Hypoosmotic stress: ultrapure water-diluted medium, hyperosmotic stress: mannitol-supplemented medium, DIC: differential interference contrast, white bar: 20 μm. n = 12–16 cells (pooled from 4 independent experiments). Note that the signal intensity of DIC cannot be compared among the images. (**C** and **D**) A computational simulation for the relationship between the grid space and the number/size of ASK3 clusters. Pale red shading: the assumed range corresponding to hyperosmotic stress (details in Supplementary Text), dashed line: the minimum of clusters definition. Data: mean ± SEM, n = 18. (**E**) TEM analysis with immunogold labelling for ASK3. Venus-ASK3-HEK293A cells were sampled after hyperosmotic stress (800 mOsm, 3 hr). White bar: 250 nm. (**F**) Dynamics and fusion of ASK3 condensates in Venus-ASK3-HEK293A cells. Hyperosmotic stress: 500 mOsm, white bar: 2 μm. (**G** and **H**) A computational prediction for the number/size of ASK3

935   clusters after grid space expansion. Pale red dashed line: the initial values, black dashed
936   line: the minimum of clusters definition. Data: mean ± SEM, $n = 12$. (**I** and **J**)
937   Reversibility of ASK3 condensates in EGFP-FLAG-ASK3-transfected HEK293A cells.
938   After hyperosmotic stress (600 mOsm, 20 min), the extracellular osmolality was set back
939   to the isoosmotic condition. White bar: 20 μm. Data: mean ± SEM, $n = 8$ cells (pooled
940   from 3 independent experiments). (**K** and **L**) FRAP assay for ASK3 condensates in
941   ASK3-tdTomato-transfected HEK293A cells. Prior to the assay, cells were exposed to
942   hyperosmotic stress (600 mOsm, 30 min). White bar: 20 μm. Data: mean ± SEM, $n = 15$
943   cells (pooled from 5 independent experiments). (**M** and **N**) ASK3 condensation in vitro.
944   Control: 150 mM NaCl, 20 mM Tris (pH 7.5), 1 mM DTT, 15-min incubation on ice.
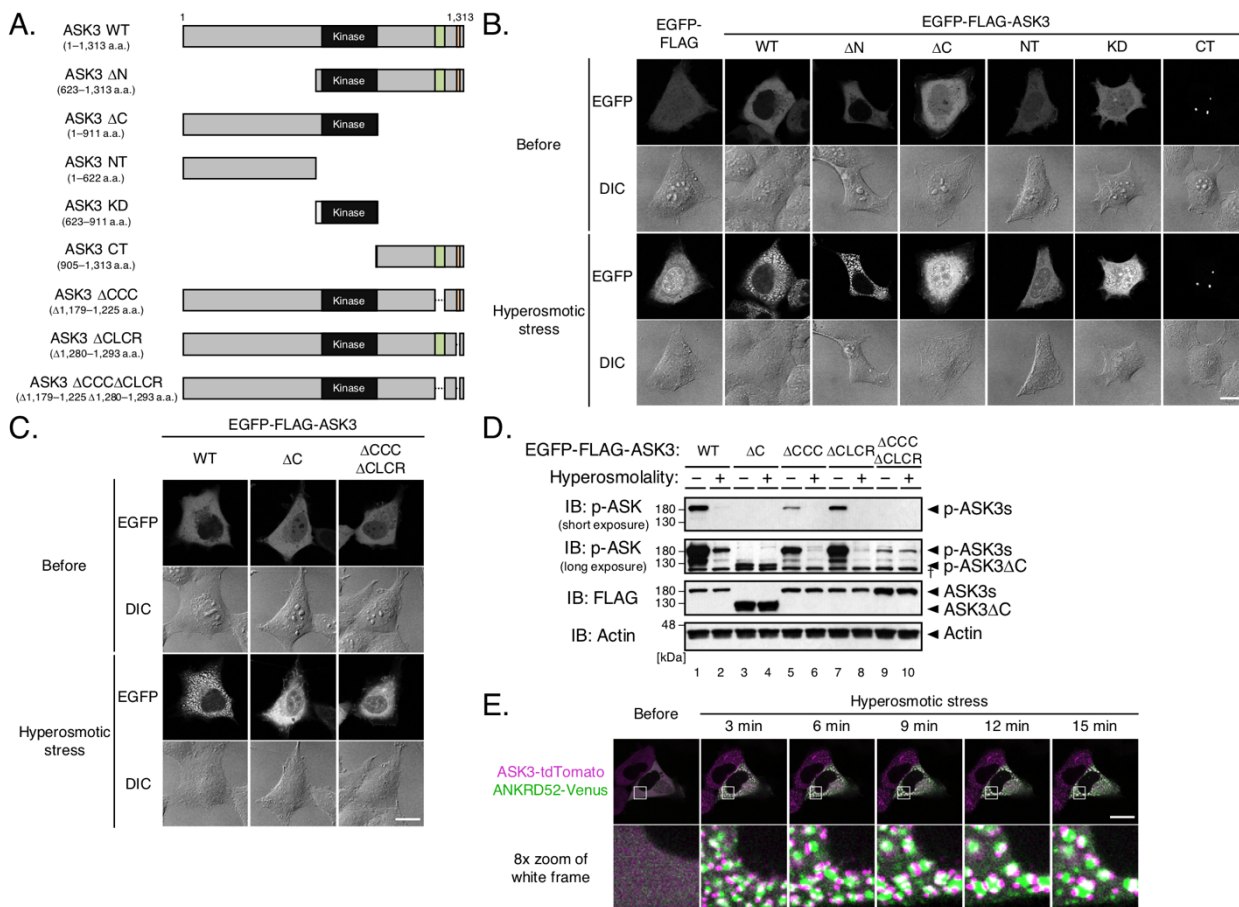945   White bar: 10 μm. Data: mean ± SEM, $n = 3$.
946

Fig. 2. ASK3 condensation is required for ASK3 inactivation under hyperosmotic stress. (**A**) Schematic representation of ASK3 deletion mutants. The numbers indicate the amino acid (a.a.) positions in wild-type (WT). Black rectangle: kinase domain (652–908 a.a.), green rectangle: C-terminus coiled-coil domain (CCC: 1,179–1,225 a.a.), orange rectangle: C-terminus low complexity region (CLCR: 1,280–1,293 a.a.). (**B** and **C**) Subcellular localization of ASK3 mutants in HEK293A cells. Hyperosmotic stress: 600 mOsm, 10 min, DIC: differential interference contrast, white bar: 20 μm. Note that the signal intensity of DIC cannot be compared among the images. (**D**) Requirement of CCC and CLCR for ASK3 inactivation in HEK293A cells. Hyperosmolality (–): 300 mOsm; (+): 500 mOsm; 10 min. IB: immunoblotting. †Nonspecific bands. (**E**) Relationship between ANKRD52 and ASK3 condensates in HEK293A cells. Magenta: ASK3-tdTomato, green: ANKRD52-Venus, hyperosmotic stress: 500 mOsm, white bar: 20 μm.
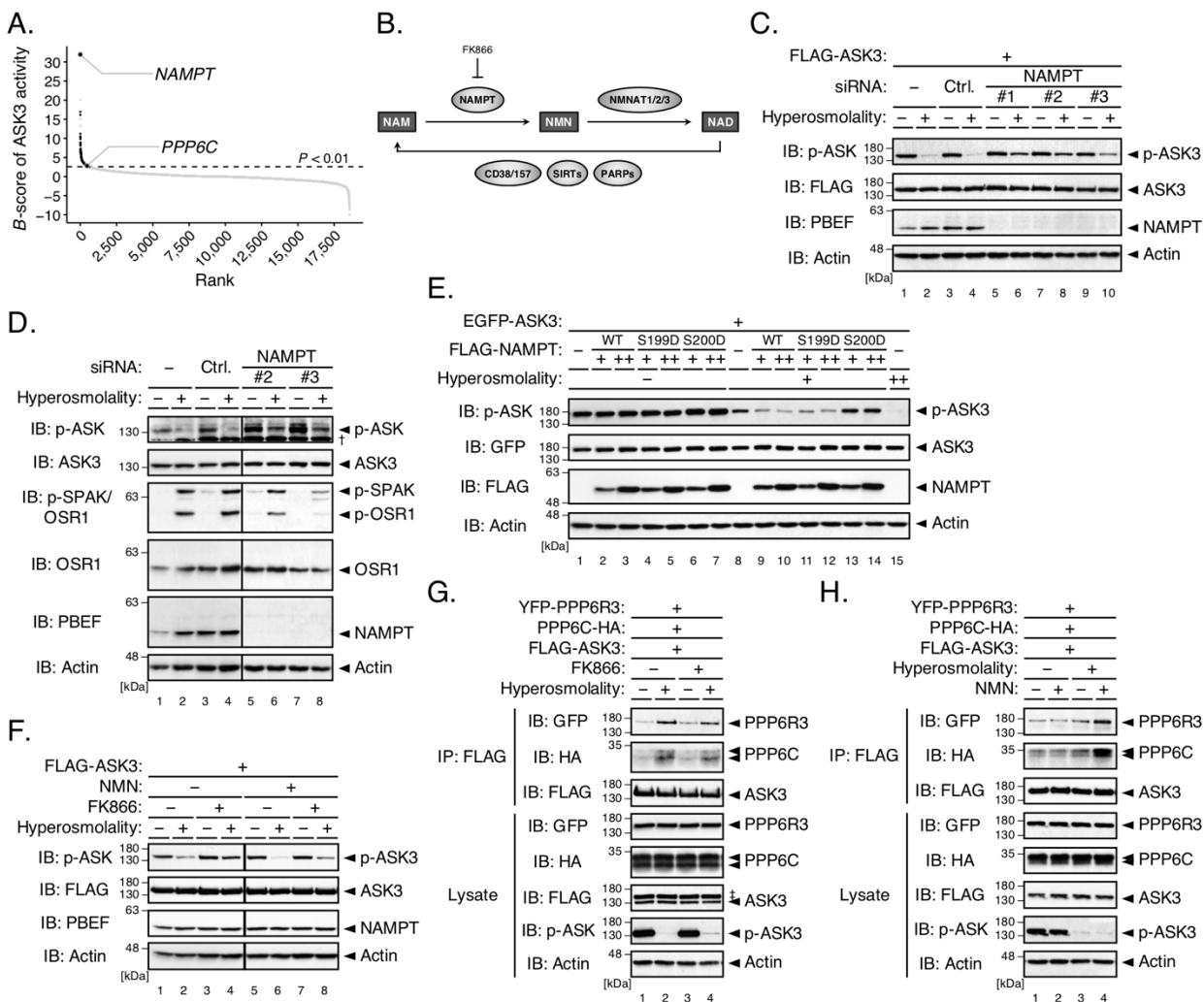
Fig. 3. The NAD salvage pathway negatively regulates ASK3 activity under hyperosmotic stress. (**A**) Distribution of gene candidates to regulate ASK3 inactivation in the previous primary screen (*17*). A sample with a higher *B*-score corresponds to a higher potential candidate. PPP6C: the catalytic subunit of PP6, an ASK3 phosphatase. (**B**) Diagram of the NAD salvage pathway. Rectangles, arrows and circles indicate NAD-related molecules, reactions and enzymes, respectively. NAM: nicotinamide, NMN: nicotinamide mononucleotide. (**C**) Effects of NAMPT depletion on ASK3 activity under hyperosmotic stress in FLAG-ASK3-stably expressing HEK293A (FLAG-ASK3-HEK293A) cells. (**D**) Effects of NAMPT depletion on endogenous ASK3 and SPAK/OSR1 activities under hyperosmotic stress in HEK293A cells. †Nonspecific bands. (**E**) Effects of NAMPT overexpression on ASK3 activity under hyperosmotic stress in HEK293A cells. WT: wild-type, S199D: homodimer-insufficient mutant, S200D: homodimer-null mutant. (**F**) Effects of FK866/NMN pretreatment on ASK3 activity under hyperosmotic stress in FLAG-ASK3-HEK293A cells. FK866: 10 nM; NMN: 1 mM; 3-hr pretreatment. (**G** and **H**) Effects of FK866/NMN pretreatment on the interaction between ASK3 and PP6 under hyperosmotic stress in HEK293A cells. FK866: 10 nM; NMN: 1 mM; 24-hr pretreatment. ‡ Remnant bands from prior detection of GFP. (**C**–**H**) Hyperosmolality (–): 300 mOsm; (+): 425 mOsm (with the exception of

980   (G and H), 500 mOsm); (++): 500 mOsm; 10 min, IB: immunoblotting, IP:

981   immunoprecipitation. Note that superfluous lanes were digitally eliminated from blot

982   images in (D and F) as indicated by black lines.
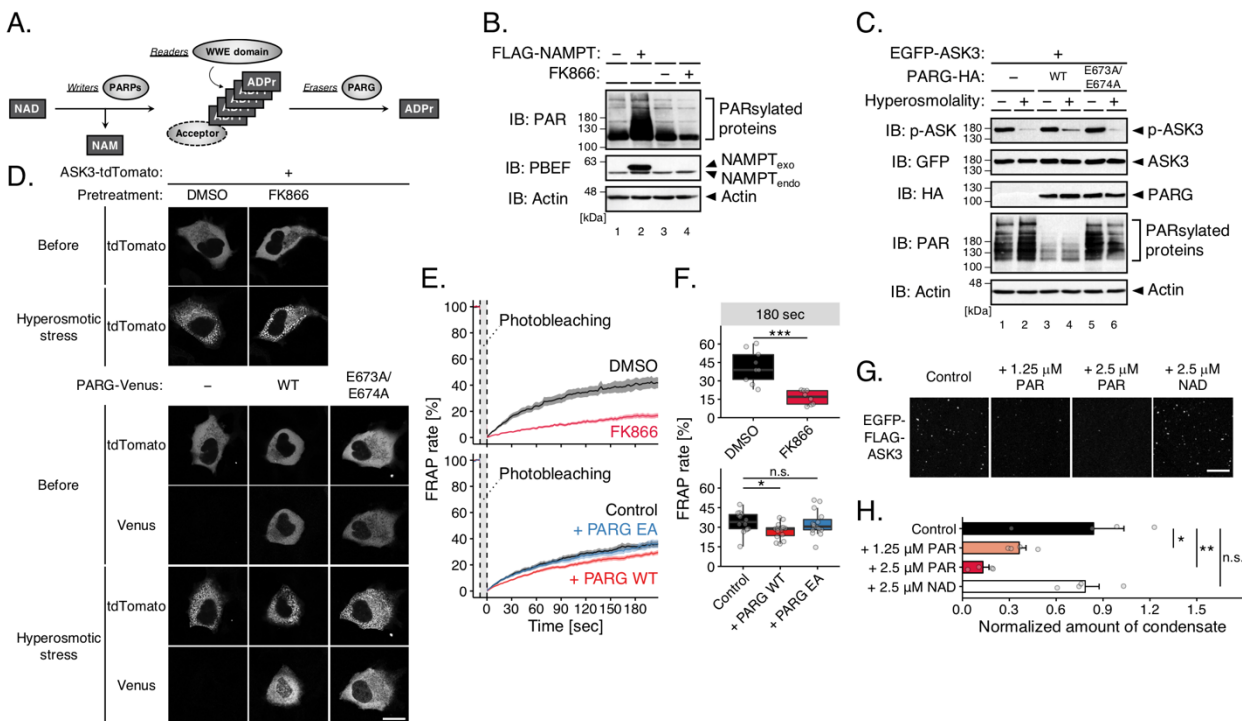
983

Fig. 4. Poly(ADP-ribose) lubricates ASK3 condensates for ASK3 inactivation. (**A**) Diagram of the PARsylation dynamics. Rectangles, arrows and circles indicate NAD-related molecules, reactions and enzymes, respectively. ADPr: ADP-ribose. (**B**) Effects of NAMPT overexpression/inhibition on the amount of PAR in HEK293A cells. FK866: 10 nM, 18–24-hr pretreatment. NAMPT$_{exo}$: exogenously expressed NAMPT, NAMPT$_{endo}$: endogenously expressed NAMPT. (**C**) Effects of PARG overexpression on ASK3 activity under hyperosmotic stress in HEK293A cells. WT: wild-type, E673A/E674A: glycohydrolase-inactive mutant. Hyperosmolality (–): 300 mOsm; (+): 425 mOsm; 10 min. IB: immunoblotting. (**D**) Effects of PAR depletion on ASK3 condensates in ASK3-tdTomato-transfected HEK293A cells. Hyperosmotic stress: 600 mOsm, 10 min, white bar: 20 μm. (**E** and **F**) Effects of PAR depletion on the FRAP of ASK3 condensates in ASK3-tdTomato-transfected HEK293A cells. Prior to the assay, cells were exposed to hyperosmotic stress (600 mOsm, 30 min). Data in (E): mean ± SEM. Top panels: n = 8–9 cells (pooled from 3 independent experiments), bottom panels: n = 14–15 cells (pooled from 5 independent experiments). *P < 0.05, ***P < 0.001, n.s. (not significant) by Brunner–Munzel's tests (with the Bonferroni correction in the bottom). (**D**–**F**) DMSO: negative control for FK866, FK866: 10 nM, 18–24-hr pretreatment, Control: empty vector transfection, PARG WT: wild-type PARG-Venus transfection, PARG EA: E673A/E674A mutant PARG-Venus transfection. (**G** and **H**) Effects of PAR on solid-like ASK3 condensation in vitro. Control: 150 mM NaCl, 20 mM Tris (pH 7.5), 1 mM DTT, 20% PEG, 15-min incubation on ice. White bar: 10 μm. Data: mean ± SEM, n = 4. *P < 0.05, **P < 0.01, n.s. (not significant) according to Dunnett's test.